Highly Sensitive, Tunable Chirality Amplification through Space Visualized for Gold Nanorods Capped with Axially Chiral Binaphthyl Derivatives

Ahlam Nemati,[†] Sasan Shadpour,[†] Lara Querciagrossa,[¶] Taizo Mori,[‡] Claudio Zannoni,[¶] and Torsten Hegmann[†§]*

[†]Advanced Materials and Liquid Crystal Institute, Chemical Physics Interdisciplinary Program, Kent State University, Kent, Ohio 44242, United States

[¶]Dipartimento di Chimica Industriale "Toso Montanari" and INSTM, Università di Bologna, Viale Risorgimento 4, IT-40136 Bologna, Italy

[‡]Graduate School of Frontier Science, The University of Tokyo, 5-1-5, Kashiwanoha, Kashiwa 277-0827, Japan

[§]Department of Chemistry and Biochemistry, Kent State University, Kent, Ohio 44242, United States

ABSTRACT: The creation and transmission of chirality in molecular systems is a well-known, widely applied notion. Our understanding of how the chirality of nanomaterials can be controlled, measured, transmitted through space, and applied is less well understood. Dynamic assemblies for chiral sensing or metamaterials engineered from chiral nanomaterials require exact methods to determine transmission and amplification of nanomaterial chirality through space. We report the synthesis of a series of GNR with a constant aspect ratio of ~ 4.3 capped with C2-symmetric, axially chiral binaphthyl thiols, preparation of dispersions in the nematic liquid crystal 5CB, measurements of the helical pitch, and the determination of the helical twisting power as well as the average distance between the chiral nanomaterial additives. By comparison to the neat organic chiral derivatives, we demonstrate how the amplification of chirality facilitated by gold nanorods decorated with chiral molecules can be used to clearly distinguish the chiral induction strength of a homologous series of binaphthyl derivatives, differing only in the length of the non-tethered aliphatic chain, in the induced chiral nematic liquid crystal phase. Considering systematic errors in sample preparation and optical measurements, these chiral molecules would otherwise be deemed identical with respect to chiral induction. Notably, we find some of the highest ever-reported values of the helical twisting power. We further support our experimentally derived arguments of a more comprehensive understanding of chirality transfer by calculations of a suitable pseudoscalar chirality indicator.

KEYWORDS: chirality amplification, gold nanorods, axial chirality, binaphthyl, liquid crystals, chiral nematic, helical twisting power, chirality indicator

Chirality is a fundamental concept of significant importance in biology, chemistry, physics, cosmology, material science, and in recent years increasingly in nanoscience.[1-9] Physical objects as well as phenomena are said to be chiral (or helical) if they cannot be precisely mapped on their mirror image by any kind of rotation or translation.[10] Chirality is observed at all length scales in nature. Yet, the origin of the universal homochirality of life is still an unsolved puzzle.[11-22] Living organisms use almost exclusively *L*-amino-acids and *D*-sugars as building blocks for proteins and nucleic acids,[23] and several types of chirality amplification through space or across length scales from solid and in several instances nanoscale surfaces to the surrounding bulk have been proposed as potential underlying causes.[15] The adornment and spatial distribution of chiral molecules around nanoscale surfaces emerged as a highly suitable approach to study amplification of chirality through space.[24-26] The distribution or dispersion of such chiral ligand-capped nanomaterials in an anisotropic liquid such as a nematic liquid crystal (N-LC) phase provides a direct visual readout (image) of the chiral induction across length scales that can be measured and compared.[27] To be specific, an achiral N-LC can be transformed into a chiral nematic LC (N*-LC) by the addition of minute amounts of a chiral solute, a so-called chiral dopant.[28-31] Addition of chiral solutes leads to a helical distortion of the one-dimensionally ordered N-LC guest molecules so that the director $\hat{n}$ describes a helix.[32] The helical pitch, p, of the induced N*-LC phase, visualized and analyzable by polarized optical microscopy, is a value that directly signifies the extent of mutually spatial molecular interactions between host N-LC and chiral solute molecules.[29] Hence, p of the induced N*-LC phase will serve as a reporter for the macroscopic chiral distortion induced by chiral molecule-decorated nanomaterials as long as the exact identical N-LC material, such as for example 5CB (Fig. 1), is used. Prior experimental evidence suggests that polyhedral, surely perceived by the surrounding N-LC molecules as quasi-spherical gold nanoparticles (Au NPs) with a NP core diameter of $\emptyset_{core} \sim 5.5$ nm capped with a cholesterol-thiol ligand shell induced almost identical p values as the neat, non-bound organic cholesterol derivative notwithstanding a one order of magnitude lower total number of chiral

cholesterol molecules in the mixture.[27] This amplification of chirality proved to be sensitive to $\emptyset_{core}$, with smaller ($\emptyset_{core}$ ~ 1.8 nm) Au NPs showing higher *p* values and larger Au NPs ($\emptyset_{core}$ ~ 10 nm) showing values of *p* that were too large to be measured.[27] In addition to the sensitivity to $\emptyset_{core}$, the amplification of chirality was shown to be even more sensitive to the shape of the nanocarriers. A comparison exclusively based on the actual number of chiral molecules in any given nanomaterial-doped 5CB mixture showed that yet another order of magnitude fewer cholesterol molecules can induce an N*-LC phase with half the *p* value when immobilized on the surface of a gold nanorod (GNR) rather than the most efficient Au NP.[33] This amplification of chirality through space has ben shown to be sensitive to the GNR aspect ratio (*AR*). We hypothesized that the spatial distribution of chiral molecules around a nanomaterial shape such as GNRs or Au NPs and a correlated, concerted action of these chiral molecules bound to one another in a sort of network through the Au–S interface augments the overall chirality transmitted to the N-LC medium.[33]

To fully quantify this chirality amplification, two key parameters need to be compared. The helical twisting power (*HTP* or β) and the distance between evenly dispersed chiral additive species ($D_{P\text{-}P}$). At sufficiently low concentrations of any given chiral additive in an N-LC, which is before *p* 'saturates', the inverse helical pitch 1/*p* increases linearly with chiral additive concentration, *c*. The slope of this line is then used to calculate *HTP*, β_W or β_{mol}: [34-35]

$$\beta_W = \frac{1}{p \cdot w_{Additive^*} \cdot r} \quad \text{or} \quad \beta_{mol} = \frac{1}{p \cdot x_{Additive^*} \cdot r} ,$$

where β_W is the *HTP* when the dimensionless weight fraction ($w_{Additive^*}$) and β_{mol} the *HTP* when the dimensionless mole fraction ($x_{Additive^*}$) of the chiral additive (or chiral ligand) is used, rather than wt.% or mol% of the whole chiral additive, and *r* given as the known enantiomeric purity of the chiral additive.[33] In this way, only chiral contributions from the organic chiral species in the N-LC mixtures are compared. Both β_W and β_{mol} are measures of a particular chiral additive's propensity in a given N-

LC host to induce a helical distortion of the director. However, only β_{mol} accounts for the number of chiral molecules present, allowing for a direct comparison of the *HTP* of a given chiral molecule in an N-LC host either dispersed as a neat organic molecule or immobilized on a nanomaterial surface with a specific shape. Any difference between two such *HTP* (β_{mol}) values is then a direct indication of the chirality amplification exerted by the nanomaterial and the collective action of all chiral molecules on its surface. The second important measure for chirality amplification through space is the calculated distance between the inducing chiral species $D_{P\text{-}P}$ (chiral molecule-capped nanomaterial or chiral molecule). $D_{P\text{-}P}$ indicates that it matters how far away on average two adjacent chiral species are while maintaining a specific value of p.[33]

While organic, molecularly dispersed chiral additives are reasonably well understood considering the wealth of specifically designed and commercially available chiral molecules, arguments vary widely on why particular types of molecules induce tighter or larger p values than others.[28, 36-39] Feringa and co-workers concluded that while no general design rules for efficient or highly potent chiral dopants can be formulated, molecular structure considerations of dopant molecules coupled to their ability to induce a certain value of p often follow specific trends, especially in a homologous series of chiral molecules.[31] Theoretical and experimental work aimed at elucidating mechanisms that result in the formation of N*-LC phases such as for example using chiral hard particle or helical particle models,[40-41] suspensions of rod-like viruses,[42] or DNA oligomers.[43] However, specific effects of subtle structural changes in a given set of chiral additives are still rather challenging to predict.

In light of the earlier reported amplification of chirality observed for GNR as carriers of chirality,[33] experimental evidence is here used to establish that such amplification can be used to distinguish the chirality and chirality transfer efficiency among a set of molecules with structural differences that would otherwise not give rise to detectable differences in p (Fig. 1A).[44] To do so, we use a series of axially chiral binaphthyl derivatives (Fig. 1B), which are well understood and intensively studied chiral additives.[36, 39, 45-49] Furthermore, binaphthyl derivatives play crucial roles as chiral C_2-symmetric ligands

in asymmetric metal catalysis.[50-53] Thus, techniques to rank their chiral interactions with surrounding molecules based on their ability to transfer chirality could be implemented in various ways into catalyst design.

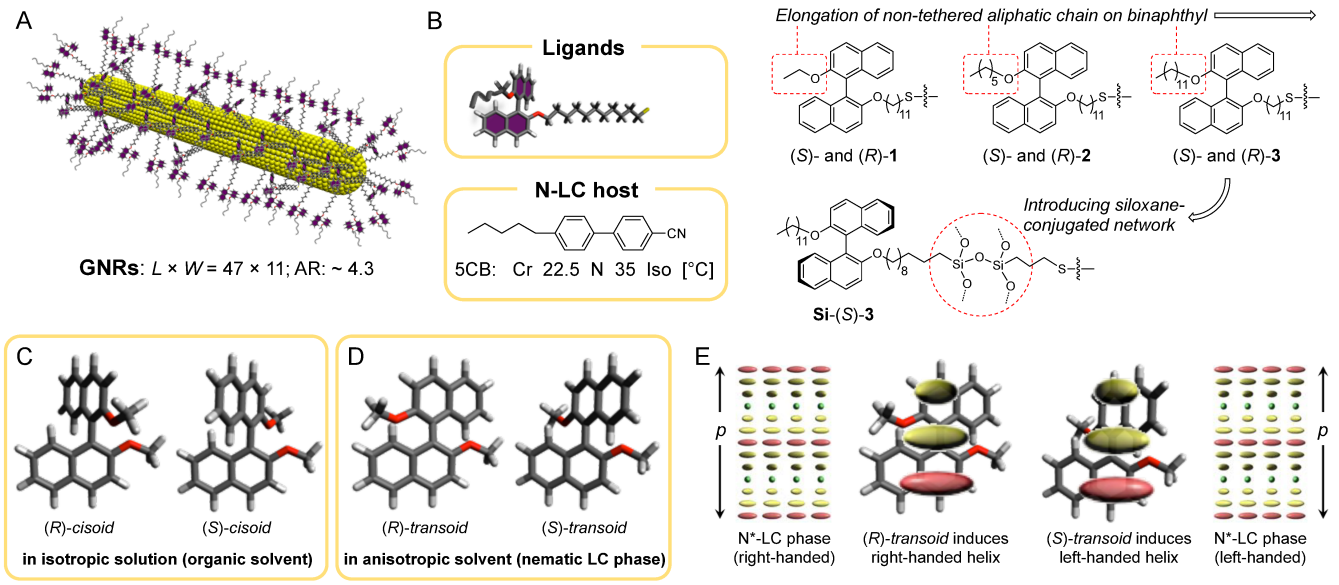

Figure 1. Materials and general considerations: (A, B) Gold nanorods (GNRs) with axially chiral binaphthyl ligands and liquid crystal (LC) host 5CB. (C) *Cisoid* conformations of non-bridged dialkyloxy binaphthyl derivatives in isotropic organic solvents and (D) *transoid* conformations in an anisotropic nematic LC solvent. (E) Handedness of the induced N*-LC phase (p = helical pitch) depending on the configuration, (*R*)- or (*S*)-, of the *transoid* conformers.[47]

Chiral binaphthyl derivatives are often synthesized and studied to control axial chirality, also called helicity, because their helicity depends on a dihedral angle between the linked naphthyl rings.[44] For a binaphthyl with (*R*)-configuration, the *cisoid* conformation (dihedral angle between 0° and 90°) gives left- handed helicity and the transoid conformation (dihedral angle between 90° and 180°) right-handed helicity, and *vice versa* for a binaphthyl with (*S*)-configuration (Figs. 1C and 1D). The dihedral angle of binaphthyl can be statically confined by a short molecular bridge between the 2- and 2'-position of the linked naphthyl rings (*e.g.*, $-OCH_2CH_2O-$) or by introducing bulky substituents.[36, 44, 47] Furthermore, the

twist sense of the induced N*-LC phase can be predicted from the configuration of the *transoid* conformers, which are predominantly formed when non-confined binaphthyl derivatives are dispersed in an N-LC medium to adopt a more rod-like overall shape commensurate with the N-LC host molecules (Fig. 1E).[47]

To validate the effect of chirality amplification, we selected three enantiomeric pairs of (*R*)-2,2'- and (*S*)-2,2'-disubstituted binaphthyls as well as one (*S*)-configuration derivative that will be bound to the GNR surface *via* a siloxane shell (Fig. 1B).[54] One aliphatic hydrocarbon chain is constant and serves as tether to the GNR surface *via* thiol binding or siloxane shell formation,[55-58] the second non-tethered aliphatic chain is varied in length. The GNRs capped with these ligands all started with the same large batch of CTAB-capped GNRs with an $AR \sim 4.3$ to ensure the only variables are related to the ligand shell itself (number of ligands and ensuing density of the ligand shell). Importantly, the *AR* of these binaphthyl-capped GNRs closely matches the $AR \sim 4.2$ of GNRs capped with a cholesterol siloxane shell studied earlier.[33] All free ligands and functionalized GNRs were then dispersed at a constant percentage by weight (0.5 wt.%) in the N-LC host 5CB. Current and prior experiments confirmed that these GNRs do not aggregate or segregate at this low concentration. While we do not assume that the GNRs are uniformly (*i.e.* spatially uniform) distributed in the induced N*-LC matrix, considerations of local anchoring of host molecules on the GNR surface, orientational flexibility of the binaphthyl ligand molecules on the GNR surface, and the Frank elastic constants of the host N*-LC medium, significant reorientations of the GNRs away from local director ($\hat{n}$) orientations can be considered negligible. Interactions between the GNRs and the elastic N*-LC medium are sufficiently strong to overcome interparticle interactions between the GNRs that would lead to appreciable GNR aggregation.[59] Several recent examples of various types of nanorods in N-LCs appear to support these assumptions especially if the surface chemistry that governs the type and strength of anchoring at the interface between the GNR ligand shell and the surrounding N-LC host molecules, is adjusted to maximize dispersion in the N-LC host.[60-64]

We then measured p of the induced N*-LC phase using two independent methods[65-66] and calculated β_{W}, β_{mol}, and $D_{\mathrm{P\text{-}P}}$. Finally, calculations of a purely geometric chirality index, $G^{\mathrm{a}}_{\mathrm{oa}}$, will be presented to support our conclusions derived from the experimental datasets.[33, 67]

RESULTS/DISCUSSION

Synthesis, characterization, and mixture preparation. The synthesis and characterization of all intermediates and chiral ligands including the (*R*)- and (*S*)- axially chiral binaphthyl derivatives with one undecylthiol and one alkyloxy aliphatic chain differing in length (ethyl, hexyl, or dodecyl) at the 2- and 2'-position of the binaphthyl, respectively ((*R*)- and (*S*)-**1**, **2** and **3**), as well as the siloxane **Si-**(*S*)-**3** and the cholesterol disulfide (**Chol-S**–)$_2$ are given in the Supporting Information (Section S1, Figs. S1-S8) and followed reported procedures.[54]

The synthesis of the chiral ligand-capped GNRs was accomplished following a procedure reported previously (Section S1, Figs. S9-S12) using a sufficiently large batch of the precursor cetyltrimethylammonium bromide (CTAB)-capped GNRs.[33] Transmission electron microscopy (TEM) revealed the dimensions (length × diameter) of the CTAB-capped GNRs (Fig. 2A). Histograms showing the length and diameter (or width) distributions are shown in Fig. S9. The average length of GNRs is 47.3 nm and the width (diameter) 11.1 nm, giving an average aspect ratio (*AR*) of ~ 4.3.

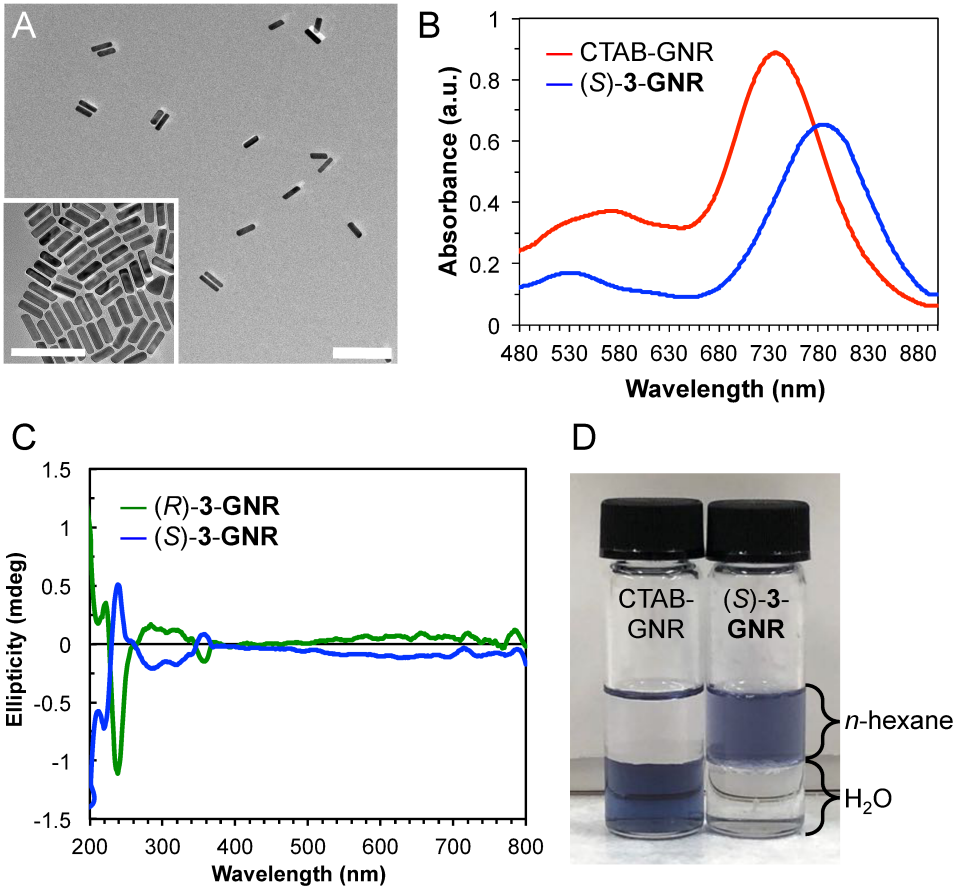

Figure 2. (A) Transmission electron microscopy (TEM) image of CTAB-GNR (scale bar = 100 nm); inset shows a magnified section of another TEM image (scale bar = 100 nm). (B) *Vis*-NIR spectra of the precursor CTAB-capped GNRs (red spectrum) in H_2O and representative for all chiral binaphthyl-capped GNRs (*S*)-**3-GNR**s in *n*-hexane (blue spectrum). (C) Solution circular dichroism (CD) spectra of (*R*)-**3-GNR** (green spectrum) and (*S*)-**3-GNR** (blue spectrum) in *n*-hexane. (D) Photograph of vials before (CTAB-capped GNRs) and after ligand exchange (here (*S*)-**3-GNR**s) after partitioning between *n*-hexane/H_2O.

Vis-NIR spectra indicate two surface plasmon resonance (SPR) bands for the CTAB-capped GNRs. After ligand exchange with the eight chiral ligands *vis*-NIR spectra show the characteristic bathochromic shift of the longitudinal SPR band from around 745 nm to 793 nm (Fig. 2B). The full UV-*vis*-NIR spectrum is shown in the Supporting Information (Fig. S11). ^{1}H NMR spectroscopy additionally shows the absence of free, non-bound ligands (Supporting Information, Fig. S12). The

circular dichroism (CD) spectra taken from the GNR solutions clearly show the mirror-imaged ligand signals for the two enantiomeric binaphthyl species attached to the GNR surface (Fig. 2C). These spectra show bands associated with the ^1B_b transition at 200 to 250 nm, the ^1L_a transition at 250 to 300 nm, and the ^1L_b transition at 300 to 350 nm of the binaphthyl moieties. The green CD spectrum for the (*R*)-configuration shows a negative to positive CD couplet for the ^1B_b transition and intense positive Cotton effects for the ^1L_a and ^1L_b transition, respectively, and *vice versa* for the blue spectrum of the (*S*)-configuration.[48, 68-69] As for numerous previously published chiral ligand-capped GNRs, no plasmonic solution CD signals were detected for the binaphthyl-capped GNRs.[70] The photograph shown in Fig. 2D provides further visual evidence of the successful phase transfer of the initially CTAB-capped GNRs (dispersed in DI H_2O) to the organic (*n*-hexane) phase after ligand exchange. The ligand coverage of the synthesized and purified GNRs was then determined by thermogravimetric analysis (TGA, Supporting Information, Fig. S13). Since the binaphthyl ligand-capped GNRs were all prepared from the exact same batch of CTAB-capped GNRs, the measured weight loss would have to be a function of M_W of the ligands and their density on the GNR surface, and the data confirm this hypothesis. The weight losses determined by TGA ranged from ~ 40% to ~ 49% for (*S*)-**1**-, (*S*)-**2**- and (*S*)-**3**-**GNR** ((*R*)-enantiomers capping the GNRs show identical values), 28% for **Si-**(*S*)-**3**-**GNR**, and 41.1% for **Chol**-**GNR** respectively.

Calculations based on the binding of the binaphthyl thiols to the curved GNR surfaces and geometrical considerations fully support both the trend in and the absolute values of the measured weight loss data (Supporting Information, Section S1, Fig. S13). Hence, experimental TGA data will be used to calculate β_W and β_{mol} and derive the amplification of chirality.

Table 1. Calculated and measured (TGA) percentage by weight (wt.%) of binaphthyl ligands on the GNR surface

GNR	**wt.%$_{Ligand*}$ (calc.)** [a]	**wt.%$_{Ligand*}$ (TGA)**
(*S*)-**1**-**GNR**	43.4 ± 8.0	39.7
(*S*)-**2**-**GNR**	46.0 ± 5.0	47.2
(*S*)-**3**-**GNR**	49.5 ± 5.0	48.6
Si-(*S*)-**3**-**GNR**	33.0 ± 10.0	28.0
Chol-**GNR**	40.0 ± 5.0	41.1

[a] The calculated wt.% range is taking the size distribution of the GNRs, as determined by TEM image analysis, into consideration.

All chiral ligand-capped GNRs and the N-LC host 5CB were dissolved in a common organic solvent (chloroform). Standard solutions of known concentrations of each were then combined to adjust the GNR concentration in 5CB to exactly 0.5 wt.% in each case. The solvent was evaporated by subjecting the open vials to a steady stream of dry nitrogen gas at 25 °C and under mild vacuum as described elsewhere in more detail.[71] For the various polarized optical microscopy (POM) and thin film induced circular dichroism (ICD) studies, the samples and substrates were prepared as specified in the Supporting Information (Section S1).

Polarized optical microscopy studies. A set of specific POM experiments was used to assess and measure the helical pitch, p, of the induced N*-LC phase. Key differences are the choice of substrates as well as interfaces and ensuing boundary conditions (Supporting Information, Section S2).[33] Figs. 3A-C depict the director field of the induced N*-phase in cells or preparations with homeotropic, hybrid or planar (homogeneous) anchoring conditions. Hybrid alignment is achieved by depositing the N*-LC material on an untreated glass slide favoring planar anchoring, and exposing the top surface to air to locally induce homeotropic anchoring.[72] Homeotropic and hybrid alignment allow for determining the

helical pitch microscopically. Cells with planar anchoring display defect textures typical for N*-LC phases with specific values of p. The oily streak and focal conic fan textures seen in Figs. 3F, 3K and 3L indicate that these N*-LC mixtures are characterized by a tight pitch.[73-75] Figs. 3D-3L shows representative photomicrographs for the (*S*)-enantiomers capping the GNRs ((*S*)-**1**-**GNR**, (*S*)-**2**-**GNR**, and (*S*)-**3**-**GNR**) dispersed in 5CB at 0.5 wt.%. 5CB doped with the same concentration of GNRs capped with the (*R*)-enantiomers ((*R*)-**1**-**GNR**, (*R*)-**2**-**GNR**, and (*R*)-**3**-**GNR**) shows practically identical photomicrographs with respect to the type of texture seen as well as the width between the dark stripes in the fingerprint textures (Supporting Information, Figs. S15-S17). The same set of images for the given boundary conditions of 5CB doped with 0.5 wt.% of **Si-**(*S*)-**3**-**GNR** is provided in Figs. 3M-3O. In all POM imaging studies, characteristic textures were obtained at 25 °C on cooling from the isotropic liquid phase. The periodic distances of disclination lines between the bright and dark areas correspond to the helical half pitch, $p/2$, in fingerprint textures of N*-LC.

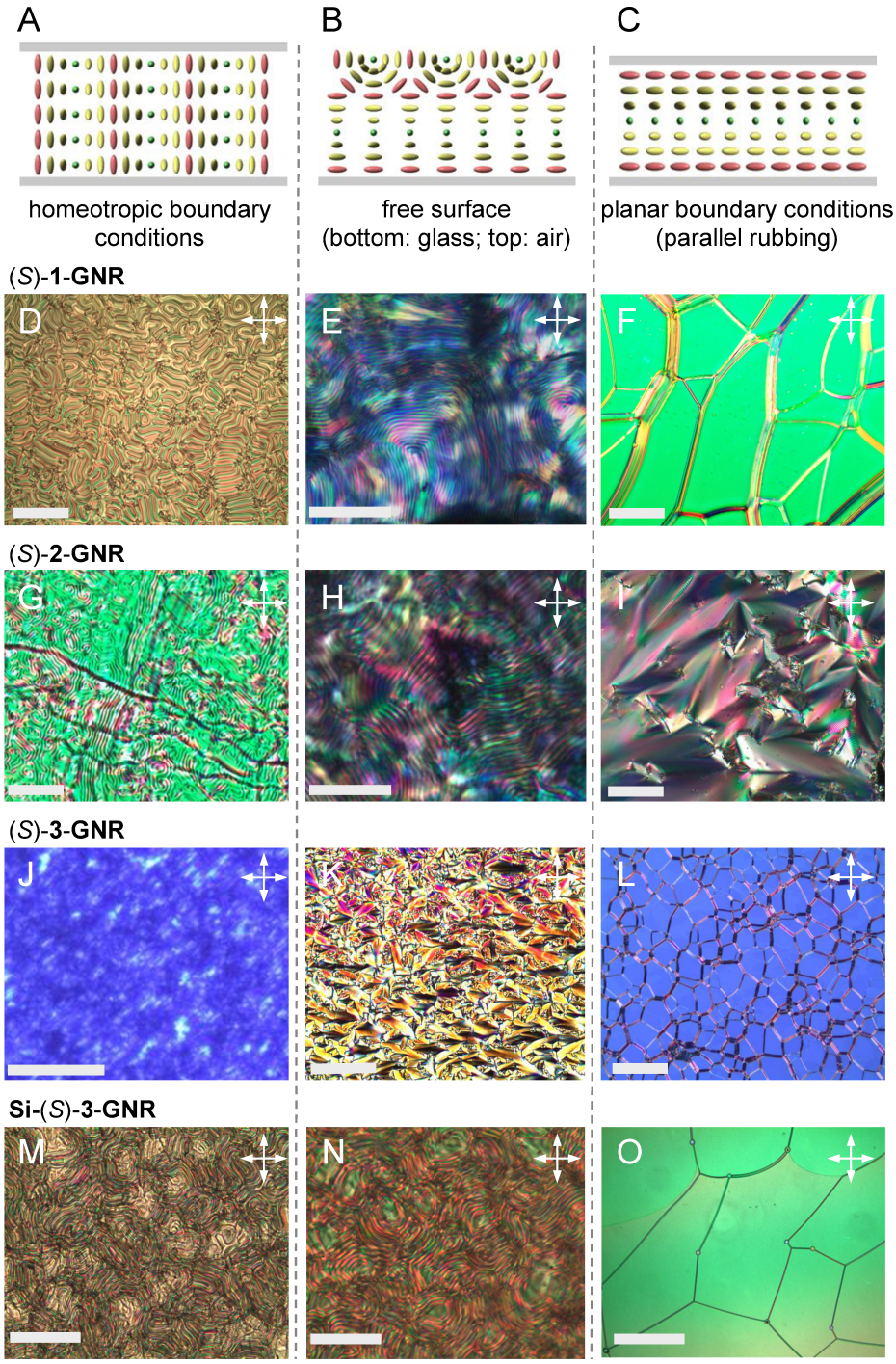

Figure 3. Schematic of the director field of N*-LC phase in sample preparations (cells) with: (A) homeotropic boundary conditions, (B) free surface, and (C) planar boundary conditions, representative for the POM images below in the same column. Polarizing optical photomicrographs (crossed polarizers) of the induced N*-LC phase induced by addition of 0.5 wt.% of the GNR in 5CB at 25 °C on cooling from the isotropic liquid phase. (D-F) (*S*)-**1-GNR**, (G-I) (*S*)-**2-GNR**, (J-L) (*S*)-**3-GNR**, and (M-

O) **Si-**(*S*)-**3**-**GNR** (all scale bars = 50 μm, cell gaps: 20 μm in planar and homeotropic cells). For POM images of the (*R*)-enantiomer GNR-doped 5CB samples, see Supporting Information, Figs. S15-S17.

POM images for cholesterol-thiol-capped GNRs (**Chol**-**GNR**), which we will later use for comparison, are given in the Supporting Information (Fig. S18). Images and microscopically determined values of *p* are given in the Supporting Information (Figs. S19-S22) and are summarized in Table 2. The N*-LC induced by (*S*)-**1**-**GNR** shown in the second row of Fig. 3 is characterized by fingerprint textures in homeotropic and free surface boundary condition, respectively (Figs. 3D and 3E). Between substrates treated to induce planar anchoring (unidirectionally rubbed polyimide), and due to the small helical pitch, oily streak textures are formed (Fig. 3F). Similar observations were made for 5CB doped with 0.5 wt.% (*S*)-**2**-**GNR** (Figs. 3G-3I) and (*S*)-**3**-**GNR** (Figs. 3J-3L). Because *p* is progressively getting tighter as the non-tethered aliphatic hydrocarbon chain on the binaphthyl ligands is elongated from C2 to C12, fan textures begin to occur more frequently for preparations favoring planar or hybrid alignment (Figs. 3I and 3K). Finally, the N*-LC induced by doping 0.5 wt.% of GNRs capped with the binaphthyl ligands featuring a siloxane inner shell (**Si-**(*S*)-**3**-**GNR**) displays fingerprint textures in homeotropic as well as hybrid boundary conditions, and planar textures with stripe defects in cells treated to induce planar anchoring. The pitch, however, is visually larger in comparison to the other three GNRs with simple aliphatic thiolate ligands.

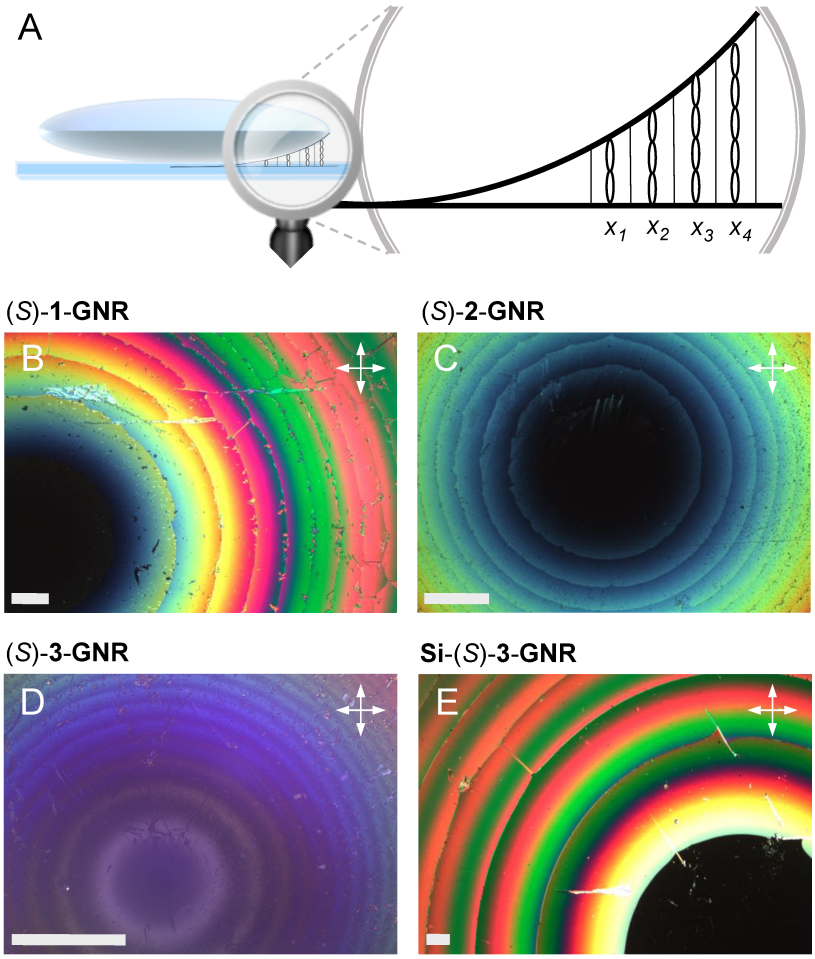

Figure 4. Schematic of the Grandjean-Cano lens experiment for determining p using a plano-convex lens and a flat glass substrate both treated with rubbed polyimide to induce planar alignment; photomicrographs (crossed polarizer) were taken at 25 °C on cooling from the isotropic liquid phase; 5CB doped with 0.5 wt.% of: (B) (*S*)-**1-GNR**, (C) (*S*)-**2-GNR**, (D) (*S*)-**3-GNR**, and (E) **Si-**(*S*)-**3-GNR** (all scale bars = 100 μm).

To verify the twist sense of the induced N*-LC phase we studied contact preparations between GNR-doped 5CB and 5CB doped with a chiral dopant known to induce a left-handed N*-LC phase (cholesteryl oleyl carbonate, COC), both doped with 0.5 wt.% (Supporting Information, Fig. S23).[54] A discontinuity in the contact zone (more precisely the formation of an achiral N-LC phase) here indicates opposite twist sense and a continuity identical twist sense. As insinuated in Fig. 1E, the contact

preparations confirmed that the twist direction of the GNRs capped with the (*R*)-configuration binaphthyl ligands is right-handed (clockwise) and left-handed (counterclockwise) for the (*S*)-configuration.

To obtain precise value of *p* for the induced N*-LC phases we next prepared a cell geometry that produces Grandjean-Cano disclination lines by injecting the N*-LC phase between a plano-convex lens and a flat glass substrate, both treated to favor planar boundary conditions (Fig. 4A). The concentric circular Cano lines in the N*-LC phase develop because of the rotary power of the N*-LC[76] and the curvature radius, *r*, of the plano-convex lens[66] (for a detailed description of the technique as well as the measurements see Supporting Information, Figs. S24-S31). Together with the calculated values for β_W and β_{mol}, Table 2 shows that the *p* values obtained from fingerprint textures and Grandjean-Cano lens experiments (Figs. 4B-4E) are in good agreement.

Induced circular dichroism (ICD). Another technique to study the induced N*-LC phase handedness and extent of chiral induction is ICD spectropolarimetry.[77-78] Thin film preparations between two quartz plates with a cell gap ~ 20 μm are rotated in 45° intervals from 0° to 315° (in the plane normal to the light beam) in order to differentiate CD absorption (reflection) from linear dichroism and birefringence.[33] Figs. 5A-5D show the averaged ICD spectra (average of spectra collected for all sample rotation angles) with prominent ICD reflection signals for samples doped with the (*S*)-enantiomers of the binaphthyl-capped GNRs. The diameter of the interrogating circularly polarized light beams is about 4 mm (spherical beam slit size) and hence larger than any specific domain size observed by POM of the same sample preparations (Figs. 5E-5H). The reflection signals start at a wavelength of ~ 320 nm (absorption edge of 5CB)[78] and cover some parts of the visible spectral range due to reflection from the tight pitch N*-LC films. The sum ICD spectrum for the N*-LC of 5CB doped with 0.5 wt.% **Si-**(*S*)-**3-GNR**, however, shows characteristic ICD absorption signals as a result of the induction of an N*-phase with larger *p*. The POM photomicrographs of the thin films of N*-LC phases between the two quartz substrates in all cases show typical N*-LC fingerprint textures, ensuring that all ICD spectra were

performed on the same type of N*-LC texture. The sum ICD spectra and individual sample rotation (linear dichroism) spectra for 5CB doped with the (*R*)-configuration binaphthyl-capped GNRs are shown in the Supporting Information (Fig. S32). The sign of all these spectra is opposite (*i.e.* positive), confirming the opposite helical twist sense derived from the miscibility tests discussed earlier.

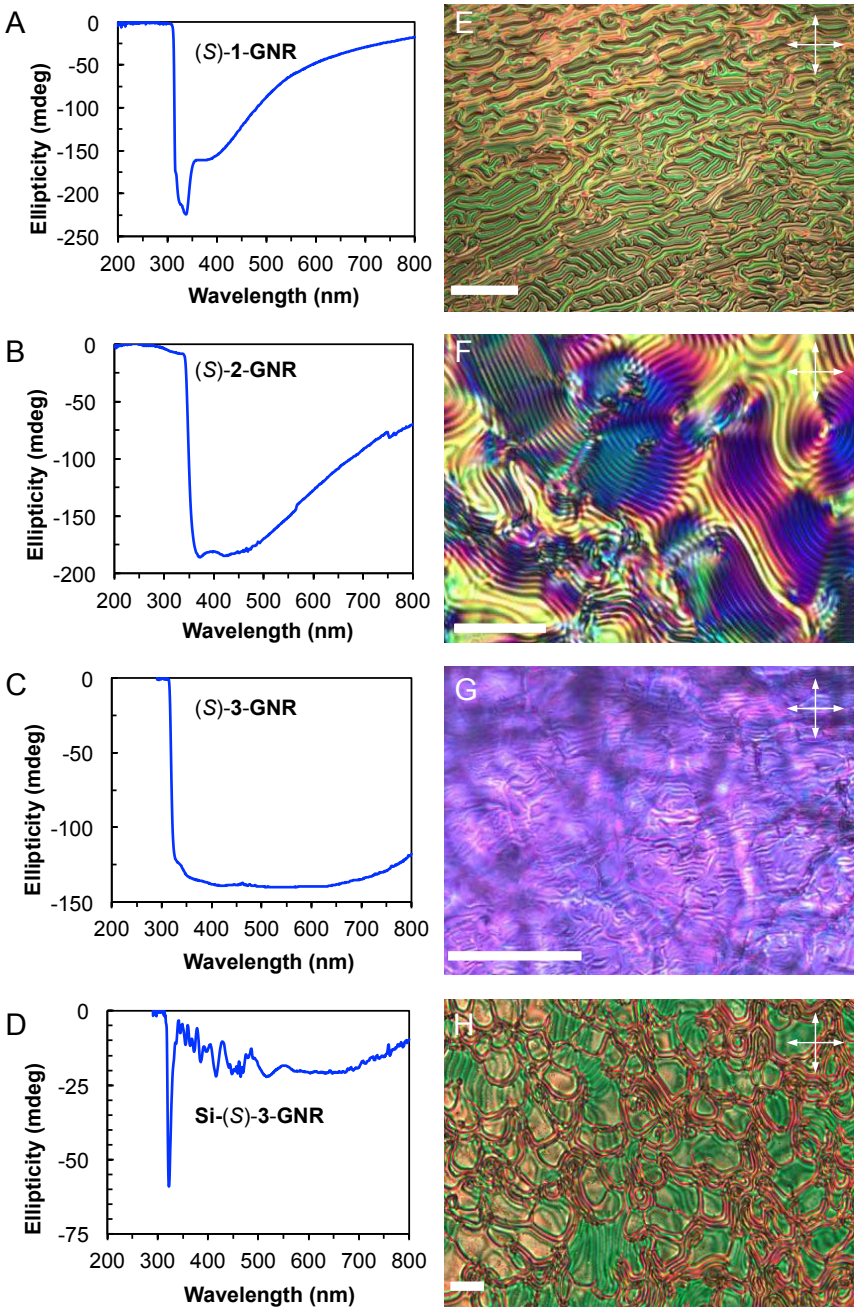

Figure 5. (A-D) Induced circular dichroism (ICD) spectra and E-H) POM photomicrographs (crossed polarizers) of 0.5 wt.% functionalized GNRs in 5CB sandwiched between two quartz substrates: (A, E) (*S*)-**1**-**GNR**, (B, F) (*S*)-**2**-**GNR**, (C, G) (*S*)-**3**-**GNR**, and (D, H) **Si-**(*S*)-**3**-**GNR** 5CB (all scale bars = 50

μm, cell gaps = 20 μm each). ICD spectra of the (*R*)-enantiomer-capped GNRs in 5CB are provided in the Supporting Information, Fig. S32).

Helical twisting power. To study and compare the extent of chirality amplification of the binaphthyl-capped GNRs solely depending on either the length of the non-tethered aliphatic chain or the mode of binding that affects the number of chiral molecules, we calculated their *HTP*, both β_W and β_{mol}.

Table 2. Weight fraction ($w_{Ligand*/w5CB}$), mole fraction ($x_{Ligand*}$), measured *p* values, helical twisting power (β_W), molar helical twisting power (β_{mol}), and particle-particle (additive*-additive*) distances (D_{P-P}) of chiral additives in 5CB at a constant percentage by weight of 0.5 wt.%

#	Chiral Additive*	($w_{Ligand*}/w_{5CB}$) × 10^{-3}	$x_{Ligand*}$ × 10^{-3}	*p* (µm) free surface	*p* (µm) Cano / lens method	*HTP*		D_{P-P} (nm) center-to-center
						β_W (µm^{-1}) [a]	β_{mol} (µm^{-1}) [a]	
1	(*S*)-**1**[54]	5.0	2.48	— [c]	20.6	–9.7	–19.6	3.4
2	(*R*)-**1**[54]	5.0	2.48	— [c]	20.4	+9.8	+19.8	3.4
3	(*S*)-**2**[54]	5.0	2.24	— [c]	12.6	–15.9	–33.1	3.5
4	(*R*)-**2**[54]	5.0	2.24	— [c]	13.7	+14.6	+30.4	3.5
5	(*S*)-**3**[54]	5.0	1.95	— [c]	12.7	–15.8	–40.4	3.6
6	(*R*)-**3**[54]	5.0	1.95	— [c]	12.4	+16.1	+41.4	3.6
7	(*S*)- or (*R*)-**1**-, **2**-, or **3**-**Au NPs**, $\emptyset_{core}$ = 1.1 – 2.5 nm[54]	1.6 – 3.0	0.59 – 1.28	11.0 – 29.5 [d]	11.8 – 27.7 [d]	7.0 – 14.5 [d] + for (*R*), – for (*S*)	61.2 – 66.2 [d] + for (*R*), – for (*S*)	4.7 – 14.0 [d]
8	(*S*)-**1**-**GNR**	2.0	1.0	5.2	5.2	–96.9	–191.8	46.5
9	(*R*)-**1**-**GNR**	2.0	1.0	4.6	5.1	+98.8	+195.6	46.5
10	(*S*)-**2**-**GNR**	2.3	1.0	2.4	2.4	–176.6	–392.6	47.2
11	(*R*)-**2**-**GNR**	2.3	1.0	2.5	2.3	+184.2	+409.6	47.2
12	(*S*)-**3**-**GNR**	2.4	0.95	1.2	0.8	–514.4	–1312	50.4

13	(*R*)-**3**-**GNR**	2.4	0.95	1.1	0.9	+457.2	+1166	50.4
14	**Si-**(*S*)-**3**-**GNR**	1.4	0.47	9.1	10.1	–70.7	–209.6	54.7
15	**Si-Chol-GNR**[33]	1.4	0.55	2.4	1.4	–510.2	–1303	54.0
16	**Chol**-**GNR**	2.0	0.85	1.3	1.1	–455.5	–1064	47.6
17	COC[33]	5.0 [b]	1.83 [b]	— [c]	27.0	–7.4	–40.4	3.7
18	R811[79]	5.0 [b]	2.74 [b]	— [c]	16.5	+12.1	+44.0	3.2
19	ZLI-4572[33]	5.0 [b]	1.92 [b]	— [c]	6.6	+30.3	+157.7	3.6

[a] The sign indicates the handedness of the induced N*-LC phase. The opposite enantiomer of a particular chiral additive molecule or additive gives the same value but opposite sign; a negative sign indicates a left-handed N*-LC phase and a positive sign a right-handed. The values were obtained using the more precise p values obtained from the Cano or lens method, respectively. [b] For $w_{\text{Ligand*}}$ and $x_{\text{Ligand*}}$ weight and M_{W} of the commercial organic chiral additives were used, although these were not as ligands. [c] For the commercially available chiral dopants as well as the free, non-bound binaphthyl derivatives only the pitch determined by the Grandjean-Cano wedge cell method was used to calculate the helical twisting power. [d] Au NPs capped with the exact same ligands, (*S*)- or (*R*)-**1**-**GNR**, (*S*)- or (*R*)-**2**-**GNR** as well as (*S*)- or (*R*)-**3**-**GNR**, range in size (core diameter) from 1.1 to 2.5 nm, and as a result thereof, their ligand coverage varies accordingly. Thus, these Au NPs are grouped together and ranges of values are provided.

A direct comparison of these values to those for the free organic chiral ligands ((*R*)- and (*S*)-**1**, **2** and **3**), commercially available chiral dopants (COC, R811[79], and ZLI4572[33]; chemical structures are provided in the Supporting Information, Section S1), cholesterol-thiol-capped **Chol-GNR**, and previously reported cholesterol-siloxane-capped GNRs (**Si-Chol-GNR**)[33] allows us to outline clear chirality amplification trends. Keeping in mind that β_{mol} takes the total number of chiral molecules into consideration for the determination of the *HTP*, β_{mol} then denotes the extent of chirality amplification through space exerted by the GNR as carriers of chirality. Using the values for the ligand coverage provided in Table 1 and the calculations and data outlined in Fig. S14 and Table S1 (Sections S1 and S3, Supporting Information), we can also determine the number of binaphthyl ligands capping the GNRs and the average distance between the chiral species in each case, $D_{\text{P-P}}$. Any discussion of chirality amplification through space needs to take the measured value for p as well as the derived values for β_{mol} and $D_{\text{P-P}}$ into consideration. With that in mind, what do the values collected in Table 2 teach us? At a

constant weight fraction (0.5 wt.%) the free binaphthyl-thiol derivatives (*R*)- and (*S*)-**1**, **2** and **3** show one major trend with respect to the induced value of *p* (entries 1-6, Table 2). Assuming that the non-tethered aliphatic chain may affect the dihedral angle of the *transoid* conformers after dispersion in the N-LC phase,[80] (*R*)- and (*S*)-**1** with the shortest non-tethered aliphatic chain (OC_2H_5) induce a larger pitch than the four derivatives with longer non-tethered (hexyloxy and dodecyloxy) chains (*R*)- and (*S*)-**2** and (*R*)- and (*S*)-**3**. The difference between the latter two is practically negligible. As signified by the given sign for *HTP* (+ for right-handed and – for left-handed) among pairs of enantiomers only the handedness of the induced N*-LC phase changes; small differences among these values could arguably be due to systematic errors in weighing and software-based measurement of the distances between fringe lines in the POM images. Considering the marginally lower mole fraction $x_{Ligand*}$ of (*R*)- and (*S*)-**3** (due to their higher molecular weight) with respect to (*R*)- and (*S*)-**2**, their molar *HTP* (β_{mol}) is slightly higher and their $D_{P\text{-}P}$ slightly larger. Practically speaking, however, these enantiomeric pairs of chiral additives should be considered virtually identical in their ability to helically distort the director of the N-LC host phase. As a proof point, immobilizing these chiral molecules on the surface of nanomaterials should allow us to distinguish their *HTP* if their chirality is amplified. First, let us consider the Au NPs, (*S*)- or (*R*)-**1**-, **2**, and **3**-**Au NP**, capped with the respective binaphthyl-thiol ligands (entry 7, Table 2). The values for *p* are virtually identical to those of the free ligands, with the smaller NPs in this series ($\emptyset_{core}$ ~ 1.1 – 1.3 nm) such as (*S*)-**2**-**Au NP** inducing a tighter pitch in 5CB than the NPs with larger core diameter ($\emptyset_{core}$ ~ 1.7 – 2.5 nm) such as (*R*)-**1**-**Au NP**.[54] While the synthesis of these Au NPs followed the exact same procedure, with the chiral binaphthyl-thiol ligands present during the one-phase Brust-Schiffrin reaction, the increasing steric demand of the ligands with longer non-tethered aliphatic chains resulted in progressively larger Au NP core diameters. Larger NP cores result in diminishing weight fractions of chiral ligand, and in turn, higher values for β_W and β_{mol}. At a constant percentage by weight, larger cores also result in larger values for $D_{P\text{-}P}$. It is therefore not surprising that the Au NPs with the largest core diameters ((*R*)-**1**- and (*R*)-**2**-**Au NP**; $\emptyset_{core}$ ~ 2.5 and 2.1 nm, respectively) show the highest

values for β_{mol} and $D_{P\text{-}P}$ (*e.g.*, 66.2 μm^{-1} and 14 nm for (*R*)-**1**-**Au NP**) and those with the smallest core diameters ((*S*)-**2**- and (*S*)-**3**-**Au NP**; $\emptyset_{core}$ ~ 1.1 nm each) the lowest values (for example, 61.2 μm^{-1} and 4.7 nm for (*S*)-**2**-**Au NP**). Nonetheless, all the binaphthyl-capped Au NPs generate elevated values for β_{mol} and $D_{P\text{-}P}$ in comparison to the free non-bound binaphthyl derivatives, clearly indicating their ability to amplify chirality in the surrounding N-LC phase.[54]

To eliminate the influence of variations in NP size and take advantage of the amplification of chirality by desymmetrization and shape complementarity[33] when quasi-spherical Au NPs are replaced by GNRs of constant *AR*, we next focus on the GNRs capped with the identical binaphthyl ligands ((*R*)- and (*S*)-**1**, **2**- and **3**-**GNR**, entries 8-13, Table 2). The weight and mole fractions of the chiral ligands on the GNR surface are almost constant. Yet, *p* drastically shrinks by ~ 50% each time the length of the non-tethered aliphatic chain of the binaphthyl ligand is reduced, resulting in *p* values of 800 and 900 nm (*i.e.* showing selective reflection at the far edge of the visible portion of the electromagnetic spectrum) for (*R*)- and (*S*)-**3**-**GNR** at 0.5 wt.% in 5CB. These values result in some of the highest ever reported values for β_W and β_{mol} when considered together with the values previously reported for the cholesterol-siloxane-capped GNRs **Si-Chol-GNR** with a near identical *AR* ~ 4.2 (entry 15, Table 2)[33] and the related cholesterol thiol-capped GNRs (**Chol-GNR**). Siloxane conjugation for the here described binaphthyl ligands such as **Si-**(*S*)-**3**-**GNR**, however, leads to larger *p* and lower β_W as well as β_{mol} values (entry 14, Table 2). This suggests that a threshold number of chiral molecules on the GNR surface are required for cooperative effects to be observed, which then lead to pronounced chiral amplification through space. From the catalogue of chiral additives listed in Table 2, **Si-**(*S*)-**3**-**GNR** has the lowest mole fraction of chiral ligands ($x_{Ligand*}$ = 0.47). Eliminating the siloxane shell by attaching cholesterol-thiols directly to the surface of the *AR* ~ 4.3 GNRs (entry 16, Table 2) leads again to smaller values for the induced helical pitch (*p* = 1.1 μm) and much larger values for β_W and β_{mol}.

A comparison with the values obtained for rather frequently used commercially available chiral additives to induce N*-LC phases (entries 17-19, Table 2; with ZLI-4572 frequently considered a

powerful chiral dopant) shows that all chiral ligand-capped GNRs described here outperform these commercial materials. As expected, the GNRs also outperform the free binaphthyls and the binaphthyl-capped Au NPs. Furthermore; the values calculated for $D_{P\text{-}P}$ of the GNRs are on the same order of magnitude than the value previously reported for **Si-Chol-GNR** (~ 46 – 50 nm from the center of one GNR to the center of the next). We effectively demonstrated how close these calculated values are to the real values by freeze-fracture TEM experiments. These TEM images supported the calculated $D_{P\text{-}P}$ values and revealed spatially twisted GNRs, supporting a chiral feedback model, where the powerful chiral GNR additives induce their own helical twist that further amplifies their chirality in the 5CB N-LC host medium.[33] Most importantly, however, through amplification of chirality by introducing GNRs as carriers of the chiral information, otherwise similarly performing chiral additives can now be easily distinguished.

While the p, β_W and β_{mol} values for (*S*)- and (*R*)-**2** and -**3** (and the values for the corresponding Au NPs) are near identical, these values differ dramatically for (*R*)- and (*S*)-**2**- and **3**-**GNR**, in most cases by well over 50%. Figure 6 underlines the discussed trends by plotting $D_{P\text{-}P}$ *vs*. β_{mol}. The enormous difference in scale between the free non-bound binaphthyl ligands (empty brown, orange and green diamonds as well as squares in the inset in Fig. 6) and the binaphthyl-capped GNRs (filled brown, orange and green diamonds as well as squares) becomes very apparent in Fig. 6. Notably, the trends in the free ligands and GNR series, indicated by the two dashed arrows, are indeed rather similar. Nevertheless, it would be a challenging task to rationalize the small differences in these values for the free non-bound chiral ligands considering unavoidable systematic errors. However, by introducing these chiral molecules into the same N-LC host immobilized on a GNR surface now allows us to argue that the likely small differences in the dihedral angle between naphthyl rings in the *transoid* conformation are amplified leading to these drastically different values for p and *HTP*.

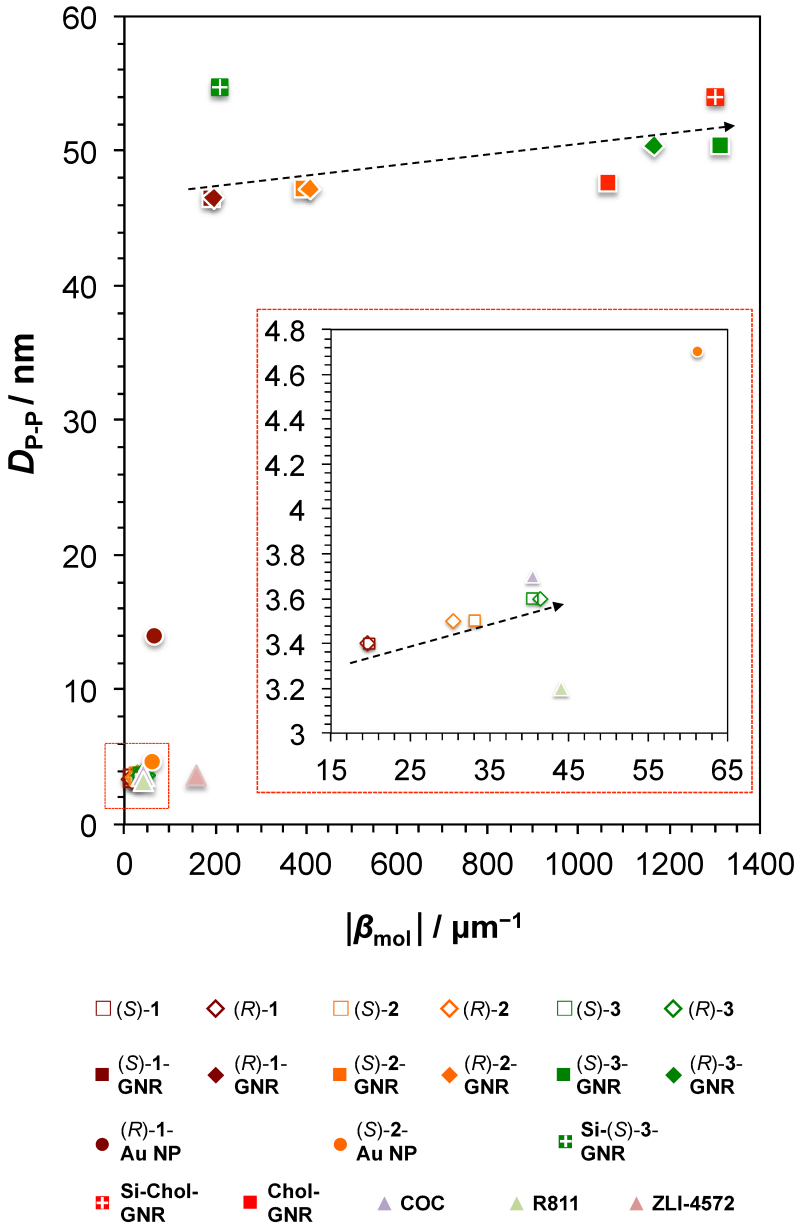

Figure 6. Chirality efficiency plot: $D_{P\text{-}P}$ *vs.* $|\beta_{mol}|$. The most efficient chiral additives occupy the top right corner of this plot, the bottom lower corner the least efficient ones. Inset shows section highlighted in the lower left section of the plot.

Given that a longer and longer non-tethered aliphatic chain (C2 to C12) will experience an increasing tendency to adopt a more rod-like shape in the N-LC host composed of rod-like 5CB molecules, the dihedral angle would have to increase. This, in turn, would lead to a tighter pitch of the induced N*-LC

phase considering arguments made in Fig. 1E. Computational approaches should help shine more light onto this.

Quantification of chirality. We have previously shown that introducing an absolute, rather than a relative to a reference[81] (such as the Hausdorff chirality measure[82-83]), pseudoscalar chirality indicator derived from the geometry of a chiral molecule[67, 84-85] or a nanoscale particle[86-87] decorated with chiral molecules gives values for a chirality index, $G_{\mathrm{oa}}^{\mathrm{a}}$, that matches extraordinarily well with the experimental data and trends of the calculated values for *HTP*. In particular, $G_{\mathrm{oa}}^{\mathrm{a}}$ allowed us to make comparisons, predictions, and draw conclusions about the chiral induction potential of chiral organic molecules as well as GNRs and polyhedral (quasi-spherical) Au NPs decorated with these exact chiral molecules.[33] This index depends solely on pure geometric information such as the position and orientation of the chiral ligand molecules with respect to the nanoparticle frame, and thus indirectly on the shape and size of the nanomaterial carrying the chiral ligand shell:[33]

$$G_{\mathrm{oa}}^{\mathrm{a}} = \sum_{P} \begin{cases} \dfrac{\left[\left(\boldsymbol{r}_{\mathrm{ij}} \times \boldsymbol{r}_{\mathrm{kl}}\right) \cdot \boldsymbol{r}_{\mathrm{il}}\right]\left(\boldsymbol{r}_{\mathrm{ij}} \cdot \boldsymbol{r}_{\mathrm{jk}}\right)\left(\boldsymbol{r}_{\mathrm{jk}} \cdot \boldsymbol{r}_{\mathrm{kl}}\right)}{N\left(\boldsymbol{r}_{\mathrm{ij}} \boldsymbol{r}_{\mathrm{jk}} \boldsymbol{r}_{\mathrm{kl}}\right)^{2} \boldsymbol{r}_{\mathrm{il}}} & \text{if } i < j < k < l \in [1, \ldots, N] \\ 0 \text{ otherwise} \end{cases}$$

where N is the total number of atoms (or beads in the case of a coarse-grained, CG, approach), P represents all permutations of i, j, k, l atoms/beads, and $\boldsymbol{r}_{\mathrm{ij}}$ is the vector distance between any two atoms i and j.

We are here using $G_{\mathrm{oa}}^{\mathrm{a}}$ to examine if changing the position, number, structure, and as a result thereof, the conformation of the chiral binaphthyl ligands on the surface of a GNR can lead to the experimentally observed changes in chirality, assuming, as reported earlier, that *HTP*, *i.e.* β_{W} and β_{mol}, is proportional to the chirality. We consider the chirality of an individual GNR capped with 20 of each of the six binaphthyl thiol ligands at a time, *i.e.* we assume that interactions between or aggregation of the GNRs are negligible as discussed earlier.[33]

Minimization of the aromatic core of the binaphthyl ligands was used to obtain the atomistic structures. At first, we omitted the chains and we performed both rigid and energy relaxed scans of the dihedral angle between the linked naphthyl groups (quantum mechanical, QM, geometry optimization using Gaussian, wB97XD/D95[88]). The most stable configuration is characterized by a dihedral angle of 78°. As Fig. 1 schematically suggests, in the fixed scan trend, the dihedral angles characterized by the greatest chirality are 62° and 122°, but with opposite sign (Supporting Information, Fig. S33). We have then added the aliphatic chains (C_2, C_6, C_{12}) in the all-*trans* configuration and keeping their conformation fixed, we have re-minimized the energy. These results highlighted the great effect the lateral chains have on the dihedral angle: increasing the chain length causes a variation of up to 20° in the dihedral angle values.

In the further modeling, we have then assumed, when approximating the structure of the binaphthyl core, a dihedral value of 122° to simulate (*R*) and (*S*) transoid conformations. The CG models were obtained representing the core of the binaphthyl ligand class with 4 CG beads, placed on each carbon atom bound to the naphthyl ether oxygen atoms, and their "*para*" counterparts on the same naphthyl ring system, respectively; while one carbon out of three was selected as CG position in the aliphatic chains. Fig. 7A compares the experimental β_{W} and β_{mol} data with the calculated $G_{\mathrm{oa}}^{\mathrm{a}}$ values for the binaphthyl thiols, considering for each case only one ligand. The dark blue empty circles and the light blue full dots, respectively, represent the data for β_{W} and β_{mol} of the free ligands (see entries 1 – 6 in Table 2).[54]

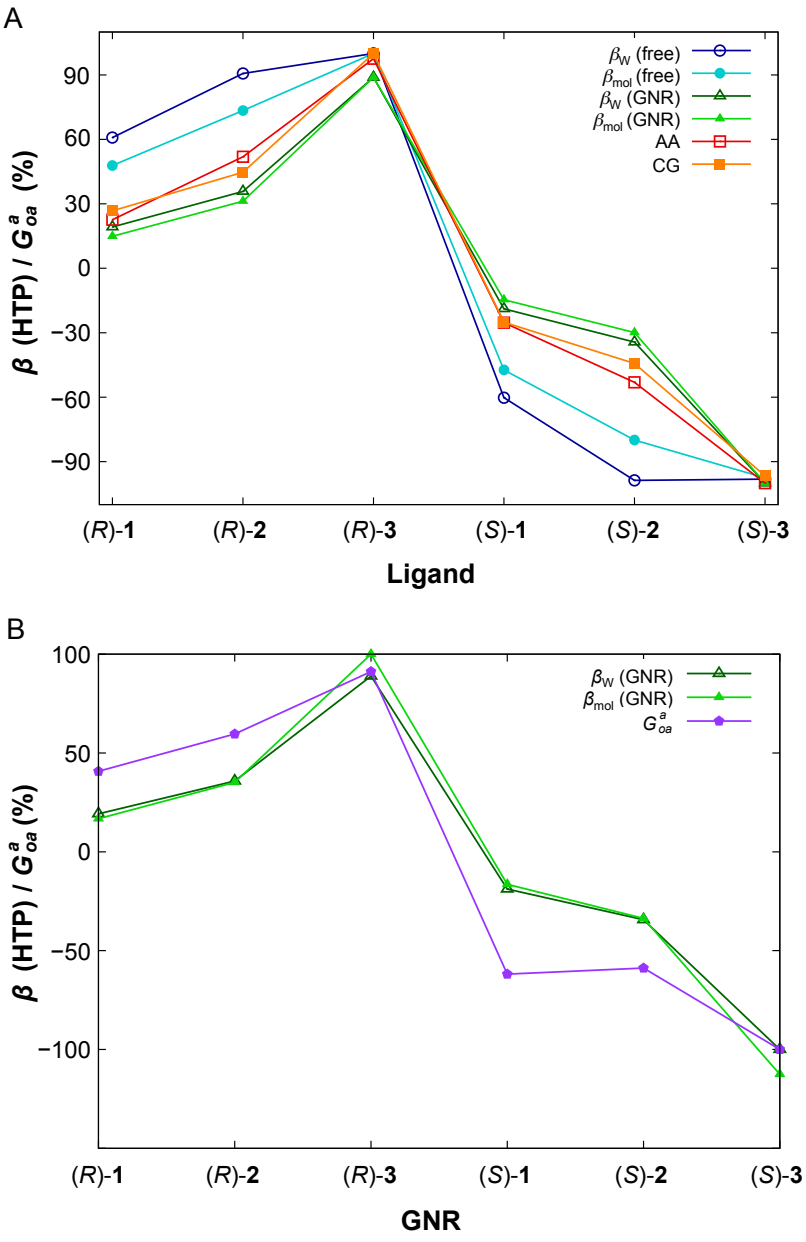

Figure 7. (A) Chirality index, G_{oa}^{a}, and helical twisting power values, β_W and β_{mol}, for the binaphthyl thiol ligands (largest values were set to 100%). (B) Values of the chirality index, G_{oa}^{a}, for 20 binaphthyl thiol ligand molecules bound to the GNR compared to the values of the experimentally determined *HTP* data, β_W and β_{mol} (largest values were set to 100%).

The dark green triangles refer to the trend of β_W obtained for the ligands capping the GNR, while the light green to β_{mol}, as reported in Table 2. Finally, empty red squares show values of overall chirality

index G_{oa}^{a} computed on atomistic (AA) structures while the full orange squares correspond to the CG representation. We see that the AA and CG are in very good agreement, apart from a scaling factor, justifying the use of the CG model in the following many ligands and multi-configuration calculation. The sign for the experimental β_{W} and calculated G_{oa}^{a} as well as overall trends appear to be consistent. In the following calculations (Fig. 7B) we choose 20 binaphthyl ligands attached to a model nanoparticle with shape and size mimicking the experimental GNR as in reference [33]. Furthermore, we selected a set of 231 configurations of the 20 ligands, by choosing positions at the top, middle and bottom of the binaphthyl-capped GNR and attaching the binaphthyl moieties perpendicular with respect to the long axis of the GNR. Taking the values of G_{oa}^{a} and β_{W} into account, the trends of experimental and computed datasets (including the sign) are in very good agreement (Fig. 7B), indicating that the calculated G_{oa}^{a} can be employed as an invaluable guide for understanding and designing chiral nanomaterials with extraordinary powerful chirality transfer ability. In particular the difference of the experimental values based on the length of the non-tethered aliphatic chain when the binaphthyl ligands are attached to the GNR surface is reproduced extraordinarily well by the calculated G_{oa}^{a} values, without any fitting parameter. It should be noted that no specific material parameter for the nature of the GNRs has been introduced. The results again suggest that the origin of the chirality amplification is arising from the fact that the chiral ligands form a network-like structure *via* the Au–S interface on the GNR surface (or *via* the siloxane network), making them act together in a correlated way, enhancing, as the experimental data suggest, the overall chirality.[33] The new data further support the firecracker ladder model proposed earlier (which provides a metaphor that it should be easier to force a helical distortion of an already twisted rope by twisting the steps)[33] considering a high local chirality of an ensemble of chiral ligands on the GNR surface that is capable of carrying a helical distortion over larger distances as suggested by the large $D_{\mathrm{P\text{-}P}}$ values. However, the current model does not capture contributions from the plasmonic nanostructures capped with the chiral ligand shell,[26] future experimental work will now focus on non-plasmonic nanoshapes with identical ligand shells with closely matching sizes and aspect ratios.

CONCLUSIONS

GNRs play an increasingly important role in the design of platforms[89] for chiral recognition, chiral sensing,[90-92] and the fabrication of metamaterials.[93-94] Intense chiroptical signals have been reported for GNRs assembled in helical[95] or side-by-side, ladder-like fashion, in some instances with very high anisotropy, g factors ($g = \Delta\varepsilon/\varepsilon$, where $\Delta\varepsilon$ and ε are the molar circular dichroism and molar extinction coefficient, respectively).[96] In the majority of these approaches, the chiral assembly of the GNRs is achieved by chiral biomolecules such as DNA,[97-98] proteins,[99] or amino acids,[100] and their proximity needs to be small and well controlled. The current work focuses on GNRs, organized in a helical fashion by the induced chiral medium, with an average inter-nanorod spacing far greater than those reported in these other examples. Here, such chiral ligand-capped GNRs are dispersed in an anisotropic fluid medium, a nematic LC phase, which serves as a reporter on their chiral induction strength. Guided by our previous findings on amplification of chirality through space by GNRs capped with a cholesterol siloxane network,[33] we provide experimental evidence that amplification of chirality by GNRs can be used to distinguish the chirality transfer and induction for a homologous series of molecules that would otherwise be regarded as equally powerful chiral inducers in the same N-LC host. To do so, we synthesized and studied a set of GNRs with identical *AR* capped with C2 axially chiral binaphthyl derivatives differing only in the length of the non-tethered aliphatic chain.

Differences in the values for p and *HTP* (both β_W and β_{mol}) measured and calculated in the induced N*-LC phase that are almost identical for the neat organic chiral molecules, when systematic errors are considered, now double and in some case near triple in value when the same chiral binaphthyl derivatives covering the surface of GNRs are dispersed in the same nematic host medium. The chirality amplification by a related series of polyhedral (quasi-spherical) Au NPs capped with these ligands only manifested itself in differences in the interparticle spacing, $D_{P\text{-}P}$, while maintaining identical values for p. For the GNRs, however, $D_{P\text{-}P}$ shows little variance, but *HTP* values are distinct for each enantiomeric

pair of ligands and are additionally among the highest ever recorded. The GNRs capped with (*S*)- and (*R*)-**3** induce exceptionally tight *p* values in the resulting N*-LC phase (as low as 800 nm) at percent mole fractions below 0.01 mole% of chiral additive molecules in the mixture. Similarly high values have only been found for GNRs capped with cholesterol derivatives.[33] The amplification effect is so sensitive that we are now able to differentiate even the most subtle structural effects of chiral additives with respect to chirality transfer. Elongation of the aliphatic chains attached at the 2- and 2'-positions of axially chiral binaphthyl derivatives should increase the dihedral angle of the *transoid* conformation when dispersed in a nematic medium. However, for the free organic binaphthyl derivatives (*R*)- or (*S*)-**1** to (*R*)- or (*S*)-**3** this change in dihedral angle appears to be too small to result in detectable changes in *HTP*. By amplifying chirality transfer through fixation of these axially chiral binaphthyl derivatives on GNR such anticipated minor changes in the dihedral angle can now be detected with great precision and certainty.

Based on these collective data we propose that the propensity of a given chiral additive in a condensed N-LC phase depends on a critical set of parameters, including previously considered specific molecular interactions reinforced by commensurate conformations of chiral dopant and host molecules, but now also including size and shape effects. We argue that the local distribution of cooperating chiral centers (or chirality) on an object with of increasing volume (or surface interacting with surrounding host molecules) with an increasingly anisometric shape results in very potent chiral inducers. Such chiral additives are then likely capable, through interactions with a large quantity of LC host molecules, to maintain the helical twist throughout this elastic medium over increasingly large distances, in part facilitated by cooperative effects among dispersed and, potentially, helically oriented chiral objects. The next logical step is to translate these findings to GNRs capped with biological relevant, hydrophilic chiral ligands in lyotropic LC systems similar to earlier studies involving Au NPs[101] and luminescent Au nanoclusters.[102] Such studies are currently underway and the data will be reported in due course.

ASSOCIATED CONTENT

Supporting Information.

The Supporting Information is available free of charge on the ACS Publications website at DOI: 10.1021/acsnano.

Materials, methods, synthesis and characterization of ligands and GNRs, additional POM and ICD data, calculations (PDF)

AUTHOR INFORMATION

Corresponding Author

*E-mail: thegmann@kent.edu

ORCID

Ahlam Nemati: 0000-0003-0282-2027

Taizo Mori: 0000-0002-6974-5137

Claudio Zannoni: 0000-0002-7977-1005

Torsten Hegmann: 0000-0002-6664-6598

Author Contributions

T.H. and A.N. conceived the experiments. A.N. and S.S. performed the synthesis and characterization of the materials. A.N. performed TEM imaging and POM experiments. A.N., S.S., and T.M. performed the calculations. L.Q. and C.Z. performed the chirality quantification calculations. T.H. and A.N. prepared the manuscript with contributions from all coauthors. T.H. directed the research. All authors have given approval to the final version of the manuscript.

Notes

The authors declare no competing financial interests.

ACKNOWLEDGMENT

This work was supported by the U.S. National Science Foundation (NSF, DMR-1506018), the Ohio Third Frontier (OTF) program for Ohio Research Scholars "Research Cluster on Surfaces in Advanced Materials" (T.H.), which also supports the Liquid Crystal Characterization facility at the Liquid Crystal Institute (Kent State University), where current TEM data were acquired. L.Q. and C.Z. thank Italian MIUR: PRIN project 2015XJA9NT for financial support. C.Z. would also like to thank the Isaac Newton Institute for Mathematical Sciences, Cambridge, UK, for support and hospitality during the program "Mathematical Design of New Materials" when work on this paper was completed. This work was supported by an EPSRC Grant.

REFERENCES

1. Knoppe, S.; Bürgi, T., Chirality in Thiolate-Protected Gold Clusters. *Acc. Chem. Res.* **2014**, *47*, 1318—1326.

2. Oh, S. S.; Demetriadou, A.; Wuestner, S.; Hess, O., On the Origin of Chirality in Nanoplasmonic Gyroid Metamaterials. *Adv. Mater.* **2013**, *25*, 612—617.

3. Ben-Moshe, A.; Maoz, B.; Govorov, A. O.; Markovich, G., Chirality and Chiroptical Effects in Inorganic Nanocrystal Systems with Plasmon and Exciton Resonances. *Chem. Soc. Rev.* **2013**, *42*, 7028—7041.

4. Wang, Y.; Xu, J.; Wang, Y.; Chen, H., Emerging Chirality in Nanoscience. *Chem. Soc. Rev.* **2013**, *42*, 2930—2962.

5. Lu, F.; Tian, Y.; Liu, M.; Su, D.; Zhang, H.; Govorov, A. O.; Gang, O., Discrete Nanocubes as Plasmonic Reporters of Molecular Chirality. *Nano Lett.* **2013**, *13*, 3145—3151.

6. Guerrero-Martinez, A.; Alonso-Gomez, J. L.; Auguie, B.; Cid, M. M.; Liz-Marzán, L. M., From Individual to Collective Chirality in Metal Nanoparticles. *Nano Today* **2011**, *6*, 381—400.

7. Dolamic, I.; Varnholt, B.; Bürgi, T., Chirality Transfer from Gold Nanocluster to Adsorbate Evidenced by Vibrational Circular Dichroism. *Nat. Commun.* **2015**, *6*, 7117.

8. Kim, Y.; Yeom, B.; Arteaga, O.; Yoo, S. J.; Lee, S. G.; Kim, J. G.; Kotov, N. A., Reconfigurable Chiroptical Nanocomposites with Chirality Transfer from the Macro- to the Nanoscale. *Nat. Mater.* **2016**, *15*, 461—468.

9. Xia, Y.; Zhou, Y.; Tang, Z., Chiral Inorganic Nanoparticles: Origin, Optical Properties and Bioapplications. *Nanoscale* **2011**, *3*, 1374—1382.

10. Kelvin, W. T. B., *The Molecular Tactics of a Crystal*. Oxford, 1894.

11. Soai, K.; Kawasaki, T.; Matsumoto, A., Asymmetric Autocatalysis of Pyrimidyl Alkanol and Its Application to the Study on the Origin of Homochirality. *Acc. Chem. Res.* **2014**, *47*, 3643—3654.

12. Viedma, C.; Cintas, P., Homochirality beyond Grinding: Deracemizing Chiral Crystals by Temperature Gradient under Boiling. *Chem. Commun.* **2011**, *47*, 12786—12788.

13. Soai, K.; Kawasaki, T.; Matsumoto, A., The Origins of Homochirality Examined by Using Asymmetric Autocatalysis. *Chem. Rec.* **2014**, *14*, 70—83.

14. Cintas, P.; Viedma, C., On the Physical Basis of Asymmetry and Homochirality. *Chirality* **2012**, *24*, 894—908.

15. Blackmond, D. G., The Origin of Biological Homochirality. *Cold Spring Harbor Perspect. Biol.* **2010**, *2*, a002147.

16. Davankov, V. A., Homochirality of Organic Matter - Objective Law or Curious Incident? *Isr. J. Chem.* **2016**, *56*, 1036—1041.

17. Kawasaki, T.; Soai, K., Amplification of Chirality as a Pathway to Biological Homochirality. *J. Fluorine Chem.* **2010**, *131*, 525—534.

18. Viedma, C.; Ortiz, J. E.; de Torres, T.; Izumi, T.; Blackmond, D. G., Evolution of Solid Phase Homochirality for a Proteinogenic Amino Acid. *J. Am. Chem. Soc.* **2008**, *130*, 15274—15275.

19. Kawasaki, T.; Suzuki, K.; Hakoda, Y.; Hatase, K.; Harada, Y.; Florini, N.; Palyi, G.; Soai, K., Chiral Crystals of Achiral Biological Compounds as an Origin of Homochirality of Biomolecules in Conjunction with Asymmetric Autocatalysis. *Origins Life Evol. Biospheres* **2009**, *39*, 289—290.

20. Davankov, V. A., Inherent Homochirality of Primary Particles and Meteorite Impacts as Possible Source of Prebiotic Molecular Chirality. *Russ. J. Phys. Chem. A* **2009**, *83*, 1247—1256.

21. Bailey, J.; Chrysostomou, A.; Hough, J. H.; Gledhill, T. M.; McCall, A.; Clark, S.; Menard, F.; Tamura, M., Circular Polarization in Star-Formation Regions: Implications for Biomolecular Homochirality. *Science* **1998**, *281*, 672—674.

22. Mason, S. F., Origins of Biomolecular Handedness. *Nature* **1984**, *311*, 19—23.

23. Hein, J. E.; Blackmond, D. G., On the Origin of Single Chirality of Amino Acids and Sugars in Biogenesis. *Acc. Chem. Res.* **2012**, *45*, 2045—2054.

24. Zhou, Y. L.; Marson, R. L.; van Anders, G.; Zhu, J.; Ma, G. X.; Ercius, P.; Sun, K.; Yeom, B.; Glotzer, S. C.; Kotov, N. A., Biomimetic Hierarchical Assembly of Helical Supraparticles from Chiral Nanoparticles. *ACS Nano* **2016**, *10*, 3248—3256.

25. Bürgi, T., Shining Light at Working Interfaces and Chiral Nanoparticles. *Chimia* **2011**, *65*, 157—167.

26. Pour, S. O.; Rocks, L.; Faulds, K.; Graham, D.; Parchansky, V.; Bour, P.; Blanch, E. W., Through-Space Transfer of Chiral Information Mediated by a Plasmonic Nanomaterial. *Nat. Chem.* **2015**, *7*, 591—596.

27. Sharma, A.; Mori, T.; Lee, H. C.; Worden, M.; Bidwell, E.; Hegmann, T., Detecting, Visualizing, and Measuring Gold Nanoparticle Chirality Using Helical Pitch Measurements in Nematic Liquid Crystal Phases. *ACS Nano* **2014**, *8*, 11966—11976.

28. Solladié, G.; Zimmermann, R. G., Liquid Crystals: A Tool for Studies on Chirality. *Angew. Chem., Int. Ed. Engl.* **1984**, *23*, 348—362.

29. Berardi, R.; Kuball, H. G.; Memmer, R.; Zannoni, C., Chiral Induction in Nematics - A Computer Simulation Study. *J. Chem. Soc. Farad. Trans.* **1998**, *94*, 1229—1234.

30. Lavrentovich, O. D.; Kleman, M. Cholesteric Liquid Crystals: Defects and Topology. In *Chirality in Liquid Crystals*; Kitzerow, H.-S.; Bahr, C., Eds.; Springer-Verlag: New York, 2001; pp. 115—158.

31. Eelkema, R.; Feringa, B. L., Amplification of Chirality in Liquid Crystals. *Org. Biomol. Chem.* **2006**, *4*, 3729—3745.

32. Fergason, J. L., Cholesteric Structure-1 Optical Properties. *Mol. Cryst.* **1966**, *1*, 293—307.

33. Nemati, A.; Shadpour, S.; Querciagrossa, L.; Li, L.; Mori, T.; Gao, M.; Zannoni, C.; Hegmann, T., Chirality Amplification by Desymmetrization of Chiral Ligand-Capped Nanoparticles to Nanorods Quantified in Soft Condensed Matter. *Nat. Commun.* **2018**, *9*, 3908.

34. Wilson, M. R.; Earl, D. J., Calculating the Helical Twisting Power of Chiral Dopants. *J. Mater. Chem.* **2001**, *11*, 2672—2677.

35. Chilaya, G., Induction of Chirality in Nematic Phases. *Rev. Phys. Appl.* **1981**, *16*, 193—208.

36. Gottarelli, G.; Hibert, M.; Samori, B.; Solladié, G.; Spada, G. P.; Zimmermann, R., Induction of the Cholesteric Mesophase in Nematic Liquid Crystals: Mechanism and Application to the Determination of Bridged Biaryl Configurations. *J. Am. Chem. Soc.* **1983**, *105*, 7318—7321.

37. Muraoka, T.; Kinbara, K.; Aida, T., Mechanical Twisting of a Guest by a Photoresponsive Host. *Nature* **2006**, *440*, 512—515.

38. Hembury, G. A.; Borovkov, V. V.; Inoue, Y., Chirality-Sensing Supramolecular Systems. *Chem. Rev.* **2008**, *108*, 1—73.

39. Li, Y.; Xue, C.; Wang, M.; Urbas, A.; Li, Q., Photodynamic Chiral Molecular Switches with Thermal Stability: From Reflection Wavelength Tuning to Handedness Inversion of Self-Organized Helical Superstructures. *Angew. Chem., Int. Ed. Engl.* **2013**, *52*, 13703—13707.

40. Dussi, S.; Dijkstra, M., Entropy-Driven Formation of Chiral Nematic Phases by Computer Simulations. *Nat. Commun.* **2016**, *7*, 11175.

41. Kolli, H. B.; Cinacchi, G.; Ferrarini, A.; Giacometti, A., Chiral Self-Assembly of Helical Particles. *Faraday Discuss.* **2016**, *186*, 171—186.

42. Tombolato, F.; Ferrarini, A.; Grelet, E., Chiral Nematic Phase of Suspensions of Rodlike Viruses: Left-Handed Phase Helicity from a Right-Handed Molecular Helix. *Phys. Rev. Lett.* **2006**, *96*, 258302.

43. De Michele, C.; Zanchetta, G.; Bellini, T.; Frezza, E.; Ferrarini, A., Hierarchical Propagation of Chirality through Reversible Polymerization: The Cholesteric Phase of DNA Oligomers. *ACS Macro Lett.* **2016**, *5*, 208—212.

44. Rosini, C.; Rosati, I.; Spada, G. P., A Conformational Analysis of Mono and Dialkyl Ethers of 2,2′-Dihydroxy-1,1′-binaphthalene by Circular Dichroism Spectroscopy and Cholesteric Induction In Nematic Liquid Crystals. *Chirality* **1995**, *7*, 353—358.

45. Hanazaki, I.; Akimoto, H., Optical Rotatory Power of 2,2'-Dihydroxy-1,1'-binaphthyl and Related Compounds. *J. Am. Chem. Soc.* **1972**, *94*, 4102—4106.

46. Gottarelli, G.; Spada, G. P.; Bartsch, R.; Solladié, G.; Zimmermann, R., Induction of the Cholesteric Mesophase in Nematic Liquid Crystals: Correlation between the Conformation of Open-Chain Chiral 1,1'-Binaphthyls and their Twisting Powers. *J. Org. Chem.* **1986**, *51*, 589—592.

47. Proni, G.; Spada, G. P.; Lustenberger, P.; Welti, R.; Diederich, F., Conformational Analysis in Solution of C2-Symmetric 1,1'-Binaphthyl Derivatives by Circular Dichroism Spectroscopy and Cholesteric Induction in Nematic Mesophases. *J. Org. Chem.* **2000**, *65*, 5522—5527.

48. Rosini, C.; Superchi, S.; Peerlings, H. W. I.; Meijer, E. W., Enantiopure Dendrimers Derived from the 1,1′-Binaphthyl Moiety: A Correlation Between Chiroptical Properties and Conformation of the 1,1′-Binaphthyl Template. *Eur. J. Org. Chem.* **2000**, *2000*, 61—71.

49. Pieraccini, S.; Gottarelli, G.; Labruto, R.; Masiero, S.; Pandoli, O.; Spada, G. P., The Control of the Cholesteric Pitch by Some Azo Photochemical Chiral Switches. *Chem.–Eur. J.* **2004**, *10*, 5632—5639.

50. Kočovský, P.; Vyskočil, Š.; Smrčina, M., Non-Symmetrically Substituted 1,1'-Binaphthyls in Enantioselective Catalysis. *Chem. Rev.* **2003**, *103*, 3213—3246.

51. Noyori, R., Asymmetric Catalysis: Science and Opportunities (Nobel Lecture 2001). *Adv. Synth. Catal.* **2003**, *345*, 15—32.

52. Tang, W.; Zhang, X., New Chiral Phosphorus Ligands for Enantioselective Hydrogenation. *Chem. Rev.* **2003**, *103*, 3029—3070.

53. Mohr, J. T.; Krout, M. R.; Stoltz, B. M., Natural products as Inspiration for the Development of Asymmetric Catalysis. *Nature* **2008**, *455*, 323—332.

54. Mori, T.; Sharma, A.; Hegmann, T., Significant Enhancement of the Chiral Correlation Length in Nematic Liquid Crystals by Gold Nanoparticle Surfaces Featuring Axially Chiral Binaphthyl Ligands. *ACS Nano* **2016**, *10*, 1552—1564.

55. Mirzaei, J.; Urbanski, M.; Kitzerow, H.-S.; Hegmann, T., Hydrophobic Gold Nanoparticles via Silane Conjugation: Chemically and Thermally Robust Nanoparticles as Dopants for Nematic Liquid Crystals. *Phil. Trans. Roy. Soc., A* **2013**, *371*, 20120256.

56. Umadevi, S.; Feng, X.; Hegmann, T., Large Area Self-Assembly of Nematic Liquid-Crystal-Functionalized Gold Nanorods. *Adv. Funct. Mater.* **2013**, *23*, 1393—1403.

57. Mirzaei, J.; Urbanski, M.; Kitzerow, H. S.; Hegmann, T., Synthesis of Liquid Crystal Silane-Functionalized Gold Nanoparticles and Their Effects on the Optical and ElectroOptic Properties of a Structurally Related Nematic Liquid Crystal. *ChemPhysChem* **2014**, *15*, 1381—1394.

58. Feng, X.; Sosa-Vargas, L.; Umadevi, S.; Mori, T.; Shimizu, Y.; Hegmann, T., Discotic Liquid Crystal-Functionalized Gold Nanorods: 2-and 3D Self-Assembly and Macroscopic Alignment as well as Increased Charge Carrier Mobility in Hexagonal Columnar Liquid Crystal Hosts Affected by Molecular Packing and pi-pi Interactions. *Adv. Funct. Mater.* **2015**, *25*, 1180—1192.

59. Liu, Q. K.; Cui, Y. X.; Gardner, D.; Li, X.; He, S. L.; Smalyukh, I. I., Self-Alignment of Plasmonic Gold Nanorods in Reconfigurable Anisotropic Fluids for Tunable Bulk Metamaterial Applications. *Nano Lett.* **2010**, *10*, 1347—1353.

60. Tasinkevych, M.; Mondiot, F.; Mondain-Monval, O.; Loudet, J. C., Dispersions of Ellipsoidal Particles in a Nematic Liquid Crystal. *Soft Matter* **2014**, *10*, 2047—2058.

61. Kubo, S.; Taguchi, R.; Hadano, S.; Narita, M.; Watanabe, O.; Iyoda, T.; Nakagawa, M., Surface-Assisted Unidirectional Orientation of ZnO Nanorods Hybridized with Nematic Liquid Crystals. *ACS Appl. Mater. Interfaces* **2014**, *6*, 811—818.

62. Liu, Q. K.; Wang, N.; Chen, P. X.; Zhang, Y.; He, S. L., Large-Area Bulk Self-Assembly of Plasmonic Nanorods in Nematic Liquid Crystal via Surface-Mediated Alignment. *Opt. Mater. Express* **2013**, *3*, 1918—1924.

63. Liu, Q.; Campbell, M. G.; Evans, J. S.; Smalyukh, I. I., Orientationally Ordered Colloidal Co-Dispersions of Gold Nanorods and Cellulose Nanocrystals. *Adv. Mater.* **2014**, *26*, 7178—7184.

64. Wang, Q.; Liu, L. Y.; Xu, L., Coupling Free Energy and Surface Anchoring Mechanism in Gold Nanorod-Nematic Liquid Crystal Dispersions. *RSC Adv.* **2018**, *8*, 4104—4111.

65. Kosa, T.; Bodnar, V. H.; Taheri, B.; Palffy-Muhoray, P., Accurate Measurement of the Helical Twisting Power of Chiral Dopants. *Mol. Cryst. Liq. Cryst.* **2001**, *369*, 129—137.

66. Heppke, G.; Oestreicher, F., Determination of the Cholesteric Screw Sense. *Mol. Cryst. Liq. Cryst.* **1978**, *41*, 245—249.

67. Pietropaolo, A.; Muccioli, L.; Berardi, R.; Zannoni, C., A Chirality Index for Investigating Protein Secondary Structures and their Time Evolution. *Proteins* **2008**, *70*, 667—677.

68. Berova, N.; Nakanishi, K.; Woody, R. W. *Circular Dichroism: Principles and Applications*, 2nd Ed.; Wiley-VCH: Weinheim, Germany, 2000.

69. Harada, N.; Nakanishi, K., *Circular Dichroic Spectroscopy: Exciton Coupling in Organic Stereochemistry*. University Science Books: 1983.

70. Li, Y. N.; Yu, D. S.; Dai, L. M.; Urbas, A.; Li, Q. A., Organo-Soluble Chiral Thiol-Monolayer-Protected Gold Nanorods. *Langmuir* **2011**, *27*, 98—103.

71. Sharma, A.; Urbanski, M.; Mori, T.; Kitzerow, H.-S.; Hegmann, T., Metallic and Semiconductor Nanoparticles in Liquid Crystals. In *Particles in Liquid Crystals*; Lagerwall, J. P. F.; Scalia, G., Eds.; World Scientific: Singapore, 2016; vol. 2, ch. 14, pp 497—535.

72. Lewis, M. R.; Wiltshire, M. C. K., Hybrid Aligned Cholesteric - a Novel Liquid-Crystal Alignment. *Appl. Phys. Lett.* **1987**, *51*, 1197—1199.

73. Demus, D.; Richter, L., *Textures of Liquid Crystals*. 1st Ed.; Deutscher Verlag für Grundstoffindustrie: Leipzig, 1978, pp 1—228.

74. Dierking, I., *Textures of Liquid Crystals*. Wiley-VCH: Weinheim, 2003; ch. 5, pp 51—74.

75. Goodby, J. W., Introduction to Defect Textures in Liquid Crystals. In *Handbook of Visual Display Technology,* Chen, J.; Cranton, W.; Fihn, M., Eds.; Springer Verlag: Berlin, Heidelberg; vols. 1-4, 2012, pp 1289—1314.

76. DeVries, H., Rotatory Power and Other Optical Properties of Certain Liquid Crystals. *Acta Crystallogr.* **1951**, *4*, 219—226.

77. Saeva, F. D.; Wysocki, J. J., Induced Circular Dichroism in Cholesteric Liquid Crystals. *J. Am. Chem. Soc.* **1971**, *93*, 5928—5929.

78. Qi, H.; O'Neil, J.; Hegmann, T., Chirality Transfer in Nematic Liquid Crystals Doped with (*S*)-Naproxen-Functionalized Gold Nanoclusters: An Induced Circular Dichroism Study. *J. Mater. Chem.* **2008**, *18*, 374—380.

79. Masahiro Mitsubishi Gas Chemical Co. Inc. Optically active compound and liquid crystal composition containing the compound. European Patent EP1270542A1 (**2003**).

80. Mori, T.; Kyotani, M.; Akagi, K., Helicity-Controlled Liquid Crystal Reaction Field using Nonbridged and Bridged Binaphthyl Derivatives Available for Synthesis of Helical Conjugated Polymers. *Macromolecules* **2008**, *41*, 607—613.

81. Dryzun, C.; Avnir, D., Chirality Measures for Vectors, Matrices, Operators and Functions. *ChemPhysChem* **2011**, *12*, 197—205.

82. Buda, A. B.; Derheyde, T. A.; Mislow, K., On Quantifying Chirality. *Angew. Chem., Int. Ed. Engl.* **1992**, *31* (8), 989—1007.

83. Gilat, G., On Quantifying Chirality - Obstacles and Problems Towards Unification. *J. Math. Chem.* **1994**, *15*, 197—205.

84. Osipov, M. A.; Pickup, B. T.; Dunmur, D. A., A New Twist to Molecular Chirality - Intrinsic Chirality Indexes. *Mol. Phys.* **1995**, *84*, 1193—1206.

85. Neal, M. P.; Solymosi, M.; Wilson, M. R.; Earl, D. J., Helical Twisting Power and Scaled Chiral Indices. *J. Chem. Phys.* **2003**, *119*, 3567—3573.

86. Almeida, A.; Querciagrossa, L.; Silva, P.; Gonçalves, F.; Canejo, J.; Almeida, P. L.; Godinho, M. H.; Zannoni, C., Reversible Water Driven Chirality Inversion in Cellulose-based Helices from Erodium Awns. *Soft Matter* **2019**, *15*, 2838—2847.

87. Berardi, R.; Cainelli, G.; Galletti, P.; Giacomini, D.; Gualandi, A.; Muccioli, L.; Zannoni, C., Can the pi-Facial Selectivity of Solvation be Predicted By Atomistic Simulation? *J. Am. Chem. Soc.* **2005**, *127*, 10699—10706.

88. Frisch, M. J.; Trucks, G. W.; Schlegel, H. B.; Scuseria, G. E.; Robb, M. A.; Cheeseman, J. R.; Scalmani, G.; Barone, V.; Mennucci, B.; Petersson, G. A.; Nakatsuji, H.; Caricato, M.; Li, X.; Hratchian

H. P.; Izmaylov, A. F.; Bloino, J.; Zheng, G.; Sonnenberg, J. L.; Hada, M.; Ehara, M. *et al*., Gaussian 09 (Gaussian, Inc., Wallingford CT, **2009**).

89. Govorov, A. O.; Fan, Z. Y., Theory of Chiral Plasmonic Nanostructures Comprising Metal Nanocrystals and Chiral Molecular Media. *ChemPhysChem* **2012**, *13*, 2551—2560.

90. Wang, Y. W.; Zhou, X. J.; Xu, C. L.; Jin, Y.; Li, B. X., Gold Nanorods as Visual Sensing Platform for Chiral Recognition with Naked Eyes. *Sci. Rep.* **2018**, *8*, 5296.

91. Kumar, J.; Erana, H.; Lopez-Martinez, E.; Claes, N.; Martin, V. F.; Solis, D. M.; Bals, S.; Cortajarena, A. L.; Castilla, J.; Liz-Marzán, L. M., Detection of Amyloid Fibrils in Parkinson's Disease using Plasmonic Chirality. *Proc. Natl. Acad. Sci. U. S. A.* **2018**, *115*, 3225—3230.

92. Funck, T.; Nicoli, F.; Kuzyk, A.; Liedl, T., Sensing Picomolar Concentrations of RNA Using Switchable Plasmonic Chirality. *Angew. Chem., Int. Ed. Engl.* **2018**, *57*, 13495—13498.

93. Greybush, N. J.; Pacheco-Peña, V.; Engheta, N.; Murray, C. B.; Kagan, C. R., Plasmonic Optical and Chiroptical Response of Self-Assembled Au Nanorod Equilateral Trimers. *ACS Nano* **2019**, *13*, 1617—1624.

94. Lan, X.; Liu, T. J.; Wang, Z. M.; Govorov, A. O.; Yan, H.; Liu, Y., DNA-Guided Plasmonic Helix with Switchable Chirality. *J. Am. Chem. Soc.* **2018**, *140*, 11763—11770.

95. Querejeta-Fernandez, A.; Chauve, G.; Methot, M.; Bouchard, J.; Kumacheva, E., Chiral Plasmonic Films Formed by Gold Nanorods and Cellulose Nanocrystals. *J. Am. Chem. Soc.* **2014**, *136*, 4788—4793.

96. Wakabayashi, M.; Yokojima, S.; Fukaminato, T.; Shiino, K.; Irie, M.; Nakamura, S., Anisotropic Dissymmetry Factor, *g*: Theoretical Investigation on Single Molecule Chiroptical Spectroscopy. *J. Phys. Chem. A* **2014**, *118*, 5046—5057.

97. Chen, Z.; Choi, C. K. K.; Wang, Q. B., Origin of the Plasmonic Chirality of Gold Nanorod Trimers Templated by DNA Origami. *ACS Appl. Mater. Interfaces* **2018**, *10*, 26835—26840.

98. Kneer, L. M.; Roller, E. M.; Besteiro, L. V.; Schreiber, R.; Govorov, A. O.; Liedl, T., Circular Dichroism of Chiral Molecules in DNA-Assembled Plasmonic Hotspots. *ACS Nano* **2018**, *12*, 9110—9115.

99. Shinmori, H.; Mochizuki, C., Strong Chiroptical Activity from Achiral Gold Nanorods Assembled with Proteins. *Chem. Commun.* **2017**, *53*, 6569—6572.

100. Han, B.; Zhu, Z. N.; Li, Z. T.; Zhang, W.; Tang, Z. Y., Conformation Modulated Optical Activity Enhancement in Chiral Cysteine and Au Nanorod Assemblies. *J. Am. Chem. Soc.* **2014**, *136*, 16104—16107.

101. Bergquist, L.; Hegmann, T., Chiral Amplification by *L*-Cysteine-Capped Gold Nanoparticles in Lyotropic Chromonic Liquid Crystals. *ChemNanoMat* **2017**, *3*, 863—868.

102. Shadpour, S.; Vanegas, J. P.; Nemati, A.; Hegmann, T., Amplification of Chirality by Adenosine Monophosphate-Capped Luminescent Gold Nanoclusters in Nematic Lyotropic Chromonic Liquid Crystal Tactoids. *ACS Omega* **2019**, *4*, 1662—1668.

TOC Figure